

Title	The tilted Iceland Plume and its effect on the North Atlantic evolution and magmatism
Creators	Celli, Nicolas Luca and Lebedev, Sergei and Schaeffer, Andrew J. and Gaina, Carmen
Date	2021
Citation	Celli, Nicolas Luca and Lebedev, Sergei and Schaeffer, Andrew J. and Gaina, Carmen (2021) The tilted Iceland Plume and its effect on the North Atlantic evolution and magmatism. (Preprint)
URL	https://dair.dias.ie/id/eprint/1129/

The tilted Iceland Plume and its effect on the North Atlantic evolution and magmatism

Nicolas Luca Celli^{a,1}, Sergei Lebedev^a, Andrew J. Schaeffer^b, Carmen Gaina^{c,d}

^a*Dublin Institute for Advanced Studies, Dublin, Ireland*

^b*Geological Survey of Canada, Pacific Division, Sidney Subdivision, Natural Resources Canada*

^c*Centre for Earth Evolution and Dynamics (CEED), University of Oslo, Oslo, Norway*

^d*School of Earth and Atmospheric Sciences, Queensland University of Technology, Australia.*

Abstract

Iceland and the encompassing Northeast Atlantic are characterized by abundant volcanism, anomalously high topography and, in many places, anomalously thick basaltic crust. This has been attributed to the Iceland Plume, rising from the deep mantle, though its structure and very existence are debated. Using seismic waveform tomography with massive datasets, we compute a new, detailed model of the crust and upper mantle beneath Iceland and the surrounding North Atlantic region. The model reveals a large, low-velocity anomaly, indicative of high temperatures, at 400-660 kilometers depth beneath eastern Greenland, where seismic receiver functions also indicate an extensive high-temperature region. The anomaly rises upwards and eastwards toward Iceland, deflecting around the thick lithosphere of Greenland's cratons, which we also image in detail. We interpret the major low-velocity anomaly as the Iceland Plume, ascending from under Greenland and captured by the Mid-Atlantic Ridge. The ascent of the plume beneath the western Northeast Atlantic is consistent with its thin lithosphere, documented by our tomography, and abundant seamounts. Our results reconcile previously contrasting views on the structure of the Iceland Plume: while the plume is clearly visible in the transition zone

*Corresponding author

Email address: nlscelli@gmail.com (Nicolas Luca Celli)

beneath Greenland, it is confined to the upper mantle beneath Iceland

Keywords: waveform tomography, Iceland, mantle plumes, plume-lithosphere interaction

The Iceland Hotspot is believed to have affected the Cenozoic evolution of the entire Northeast Atlantic region, producing large volumes of thickened crust and the intraplate basalts of the North Atlantic Igneous Province (NAIP)[1]. Since the 1970s[2, 3], these features have been interpreted as the signature of the Iceland mantle plume, but the plume’s structure and very existence remain uncertain until now. Seismic tomography is sensitive to the compositional and temperature variations of the mantle and can detect the thermal anomalies expected within mantle plumes[4]. The sparse and uneven distribution of seismic stations in the Northeast Atlantic, however, has posed a challenge for tomographic imaging. While early body-wave studies reported evidence for a vertically elongated, low-velocity anomaly under Iceland[5, 6, 7, 8], there is little agreement on how broad the inferred hot anomaly is[8, 9, 10], where it rises from[7, 11, 12], whether it is a mantle plume at all[11, 13, 14, 15] and if so, how many plumes there are[9, 10, 16, 17].

15

Iceland is located on the only portion of the Mid Atlantic Ridge (MAR) above sea level and is characterized by anomalously thick crust[18], high topography[19, 20] and flood basalts (Fig. 1) with chemical signatures similar to the NAIP volcanics[3, 21, 1, 22] that set them apart from the mid ocean ridge basalts. Iceland’s anomalous features have long been related to the ridge interacting with the anomalously hot mantle, attributed to a mantle plume on the basis of geochemistry[3, 21], seismic tomography[5, 7, 16] and numerical modelling[23, 17].

The NAIP intraplate basalts are unevenly spread across a very wide area and over a 20 Myr time span, with simultaneous magmatic episodes occurring, at times, thousands of kilometres apart[1, 24, 25]. Additionally, the distribution of Cenozoic uplift in the Northeast Atlantic shows similar complexity[26],

25

with proposed pulsed, plume-related doming as far south as the British Isles[27]. These observations have been difficult to reconcile with the classical view[2] of a
30 single, narrow, vertical plume, with recent work proposing additional complexities in its structure to explain the data[28, 23]. This, together with the varying resolution[13] of available tomographic models, limited by the highly uneven data sampling, lead to a variety of proposed models, invoking the contribution of additional other plumes under Jan Mayen[10] and the Azores[17], or an upper
35 mantle, non-plume origin of the Iceland anomaly[22, 11, 14, 15].

Recent tomographic images[29, 10, 16] show complex—and often mutually inconsistent—low velocity structures under Iceland that depart significantly from the classical plume view[2]. In the upper mantle, asthenospheric fingers
40 from the Iceland Plume have been proposed to reach southern Norway and the Irish Sea[30, 10] at present, and the Baffin Bay during the Paleogene[23]. In the deep mantle, the plume has been proposed to tilt to the south-east with increasing depth[12, 10, 16], possibly linking Iceland to the African Large Low Shear Velocity Province at the core-mantle boundary[19]. Anomalies in a number of
45 tomographic images[30, 10] have been interpreted as consistent with a plume under Iceland and reaching towards the Eurasian-Plate part of the Northeast Atlantic. Yet, the distribution of recent intraplate volcanism[31] indicates that the majority of intraplate seamounts have been forming, instead, on the North American Plate.

50
In this paper, we use waveform tomography with a massive dataset of regional and global seismic waveforms to compute a new *S*-wave tomographic model of the crust and upper mantle beneath the Northeast Atlantic. The increased resolution allows us to image in detail the structure of the Iceland Plume and its interaction with the lithosphere of Greenland and the MAR. After discussing the main features of the model, we compare it with recent tomographic
55 models and other, independently derived geophysical, geochemical and geological data to both validate our new inferences on the shape of the Iceland Plume

and discuss its role in the complex evolution of the Northeast Atlantic region.

60 1. Waveform tomography

NAT2021 is an azimuthally anisotropic, S -wave tomographic model of the upper mantle and transition zone (TZ) under the North Atlantic region, computed using waveform inversion of over 1.2 million global and regional seismograms from over 27000 events and 6000 stations (Fig. 2). The seismograms were
65 waveform-fitted using the Automated Multimode Inversion (AMI)[32], which inverts the surface-, S - and multiple S -wave parts of the wave train. Long period fundamental mode surface waves (provided by global measurements) constrain the deep upper mantle, while short periods (provided by short, regional paths) carry the information on the fine-scale details of the crust, mantle lithosphere
70 and shallow asthenosphere. S and multiple S waves yield structural information on the heterogeneity in the deep upper mantle and transition zone. Although the model construction is global, NAT2021 is optimized for the North Atlantic region. The data coverage in the region was been maximized by obtaining all freely available data. The model’s parametrization and regularization are specifically
75 finely-tuned for the region. Meticulous, manual quality control includes the identification of imaging artifacts and the identification and removal of the data from stations in the region that cause them. Earthquake source parameters are taken from the Global Centroid-moment-tensor (GCMT) catalogue[33] since 1994, with a distance-magnitude varying threshold[34]. As a result, each node
80 of the final tomographic model is sampled by over 25000 fits in the study area and at least 3807 globally (Fig. 2). Under the best-sampled parts of the region (USA and western Europe), the number of waveform fits sampling each node can be as high as 213872.

85 After download, we quality-control the waveforms for clipping and gaps, ensuring that the whole waveform—and especially the surface wave train—is fully recorded; after that, each trace is response corrected and downsampled to 1 Hz.

The successfully retrieved traces undergo a three-step inversion procedure. At first, we invert the seismogram using AMI[32]. AMI computes synthetic seismo-
 90 grams by modal summation and fits the surface, S- and multiple S -waves to the observed ones within a complex set of weighted time-frequency windows. By minimizing the misfit in the time domain, AMI produces for each fit a set of linear equations with uncorrelated uncertainties[35] describing the average S - and P -wave velocity variations from a 3D reference model within approximate sensi-
 95 tivity volumes[32]. In the second step, all equations are inverted jointly for the distribution of P - and S -wave velocities and 2Ψ S -wave azimuthal anisotropy in 3D[36] using LSQR[37] with smoothing and slight norm damping[35]. We parametrize the tomographic model using a dense triangular grid[38] with approximately 120 km lateral knot spacing and 18 and 10 triangular radial basis
 100 functions for S - and P -wave velocities, respectively (S -wave velocities: 7, 20, 36, 56, 80, 110, 150, 200, 260, 330, 410-, 410+, 485, 585, 660-, 660+, 809 and 1007 km; P -wave velocities: 7, 20, 36, 60, 90, 150, 240, 350, 485 and 585 km). Perturbations of the model parameters are computed with respect to the same 3D model used in AMI, which is a combination of a modified CRUST2[39] with
 105 added topography and our own global 1D mantle average[36]. In the third and final step of our inversion procedure, we identify and remove outliers, exploiting the substantial redundancy of our dataset. Outliers are mostly related to errors in the source location and origin time and station timing[40]. In order to identify these outliers, we first compute an initial tomographic model m_i , which
 110 will be polluted by such data errors. We then compute the synthetic data d_{syn} (the equations describing the average P - and S -wave variations beneath the sensitivity areas) by multiplying the initial model by the sensitivity matrix A . Finally, we compare the original d_{obs} and synthetic d_{syn} data and reject the ones with the largest misfit. This outlier-analysis procedure identifies and retains the
 115 most mutually consistent data and is effective in removing the data with large errors. Its effectiveness is confirmed, for example, by the disappearance of many obvious artifacts in the initial model, which often stand out as high-amplitude anomalies beneath some of the sources and stations.

120 The final model NAT2021 (Figs. 3, 4) is constructed with global data but
is specifically developed for and optimized within the North Atlantic region in
terms of the dataset, parametrization and regularization. Compared to our re-
cently published model of the South Atlantic region[41], for example, NAT2021
has a much finer gridding and an adapted, spatially variable regularisation
125 scheme, introduced to utilize the denser but highly uneven data sampling. Com-
pared to the previously published models of the Northeast Atlantic-Greenland
region, constructed using similar methods[34, 42], NAT2021 is constrained by
a significantly greater amount of new, regional data in the study area, which
yields a substantially higher resolution. In NAT2021, the resolution is also
130 explicitly variable and changes, laterally and vertically, in concert with data
sampling, which is implemented for the first time in full using regularization
coefficients that scale in 3D with the variations of data sensitivity, estimated
using the sensitivity-matrix column sums (appendix A, figs. S1, S2). Compared
to body-wave tomography, waveform tomography is less dependent on the dis-
135 tributions of seismic stations and the associated ray paths of the teleseismic
body waves—highly uneven in the NE Atlantic—and yields dense sampling of
the region everywhere. Compared to models computed using spectral element,
waveform simulations[10], our inversion utilizes a dataset that is larger by or-
ders of magnitude. The large amount of data provides the dense sampling that
140 is essential for the imaging of the North Atlantic Ocean and Greenland, where,
compared to the well-sampled continents, data coverage is scarcer.

2. Results

At long wavelengths, NAT2021 is consistent with previous global and re-
145 gional models[29, 10, 34, 43, 42], showing low velocities beneath the MAR—
lowest close to Iceland and the Reykjanes and Kolbeinsey Ridge—and high
velocities beneath the Baltic Shield and the North American and Greenland

Cratons (Figs. 3, 4). Under both the continents and the ocean, however, our model brings into focus fine-scale, detailed features within the lithosphere and
150 underlying mantle that were unseen or less clear in previous models.

Under the ocean, compared to recent waveform tomography models[34, 44, 43, 10] (Fig. 5), we identify more heterogeneous structure along the MAR close to Iceland. Strong low-velocity anomalies under the Reykjanes, Kolbeinsey and
155 Mohns Ridges (Figs. 1, 4) stand out compared to mid-ocean ridges on average (Fig. S3). The V_s anomaly beneath the MAR close to Iceland exceeds -8% and extends over a relatively broad region. Such velocities are indicative of decompression melting over broad areas, unusual for a slow-spreading MAR[45] but consistent with the presence of an upwelling of hotter mantle. Under the
160 Reykjanes Ridge, the very low velocities locate symmetrically around the ridge axis and are confined to depths smaller than 300 km. Under the Kolbeinsey and Mohns Ridge and next to Jan Mayen, velocity minima are located systematically west of the MAR in the 36-330 km depth range, whereas to the east of the ridge we observe average V_s or mildly positive V_s anomalies. The extinct Aegir-,
165 Baffin Bay- and Labrador Ridge are not underlain by low-velocity anomalies in the shallow upper mantle, in agreement with the ceasing of seafloor spreading at 24 and 33 Ma, respectively[46]. In the TZ, the lowest velocities locate under central eastern Greenland, from where they connect to shallower low-velocity anomalies under the North Atlantic and Baffin Bay.

170 In the lithosphere beneath Greenland, we image fine-scale structure within the North Atlantic and Rae Cratons, only recently imaged as separate[42]. In the north, we identify for the first time two, clearly separate high-velocity units within the previously proposed boundaries of the Rae Craton (Fig. 4). Because
175 the smallest, western cratonic unit partially locates underneath the extent of the Melville and Inglefield Belts (Fig. 1), we identify it as the Inglefield-Melville Craton. In southern Greenland, we image the North Atlantic Craton as a high velocity block between the coastal outcrops of the Proterozoic Nagsugtoqidian

and Ammassalik Belts, but notably not under its inferred inland extent to the
180 south. The Rae and Inglefield-Melville Cratons in the north are separated from
the North Atlantic Craton in the south by an area with much smaller positive
anomalies at 110-200 km depths (3-5% vs. 8+% dVs at 150 km) under cen-
tral Greenland. In central eastern Greenland, geochemical data indicate the
interaction of plume material and Archean crust in the Miocene[47], but the
185 adjacent fast lithosphere is thinner than most cratons. We suggest that this
thin—and possibly independent—cratonic block may have been eroded by the
Iceland Plume, similarly to the ongoing erosion of the Tanzanian Craton in
Africa[48], although we cannot rule out an earlier modification of the craton’s
lithosphere.

190

Under the Eurasian Plate, previous images from waveform tomography[10]
showed low-velocity “fingers” reaching from Iceland towards the Irish Sea and
Southern Norway, either side of a high-velocity anomaly beneath the North Sea.
NAT2021 features a broadly similar pattern, with lower velocities surrounding
195 a fast North Sea Basin at 100-200 km depth (Fig. 4). The differences between
images are, in part, due to the differences in the reference models and also due
to the horizontally polarized V_{SH} values [10] being different from the vertically
polarized V_{SV} ones, imaged here, due to radial anisotropy. Regardless of that,
the models clearly agree that the low-velocity anomalies beneath Iceland and
200 the MAR are much stronger than elsewhere within the ocean basin.

3. Discussion

3.1. *Asymmetric low velocities in the NE Atlantic upper mantle*

Our images indicate the presence of a large volume of anomalously hot man-
205 tle, located under eastern Greenland in the TZ, deflected, as it rises, primarily
to the east by the lithospheric keels of the North Atlantic and Rae Cratons, and
connecting to the anomalously low velocities under Iceland and the MAR (Fig.

6).

North of Iceland, we observe low velocities in the 36-660 km depth range (Fig. 4) that, at depths greater than 200 km, locate mostly west of the MAR, under the North American Plate (NAP). By averaging NAT2021 over oceanic lithosphere of the same age under the oceanic portions of the North American and Eurasian Plates in the Northeast Atlantic, we can see that, on average, the lithosphere and asthenosphere under the NAP is slower at all ages (Fig. 7). Subtraction of the global average, "normal cooling" velocity anomaly (Fig. S3) from the local averages shows that the mantle beneath the oceanic portion of the NAP is markedly hotter than both the average oceanic lithosphere and the Eurasian Plate oceanic lithosphere of the same age, except for the region close to the ridge axis, where the upper mantle is anomalously hot on both sides. Under the NAP, the upper mantle is anomalously slow from the lithosphere down to the TZ, consistent with the presence of the large low-velocity body we observe rooted in the TZ beneath eastern Greenland. Thinner lithosphere and hotter asthenosphere should result in more widespread decompression melting below the lithosphere-asthenosphere boundary (LAB) and, indeed, recent compilations of intraplate volcanism show a larger amount of seamount-like oceanic igneous features (SOIFs) in the western Northeast Atlantic[31]. By counting only the SOIFs on the oceanic lithosphere, 205 locate on the NAP—including the Vesteris seamount, the largest in the region—and only 104 are found on the Eurasian Plate (Fig. 7). This suggests that the distribution of intraplate volcanism is influenced by the upwelling of hot mantle we observe beneath the western part of the basin.

South of Iceland, the Reykjanes Ridge shows a strong low-velocity anomaly, symmetric relative to the ridge axis (Fig. 4). The Reykjanes Ridge has long been considered an area of plume-ridge interaction[3, 49, 50], with hot mantle flowing horizontally from Iceland[3]. Our tomographic images suggest that the plume material rises upwards and eastwards from under Greenland and then follows the MAR southwards in the shallow upper mantle to under the Reykjanes Ridge. This indicates that once the flow of the hot material reaches the

shallow asthenosphere, it is captured by the ridge and, instead of proceeding
240 further east, flows southwards along the ridge axis, channelled within the thinner lithosphere beneath it[51, 52].

3.2. *The Iceland Plume*

The complex, low-velocity body that we interpret as the seismic expression
245 of the Iceland Plume differs from the schematic image of a narrow, vertical mantle plume and, also, from many of the tomographic images published previously. The plume conduit comes into focus in our model thanks to the recently improved data coverage in the region, which our tomography has utilized. A signature of this anomaly, however, can be seen in other recent models. The
250 complexities of the plume-material flow that we resolve can also account for other geophysical and geological observations.

Many seismic studies[5, 6, 7, 10, 34, 16] detected low velocities in the mantle under Iceland, some interpreting them as a deep mantle plume and others
255 arguing, instead, that the anomaly was confined to the upper part of the upper mantle[13, 11, 8] and was not of plume origin. Our model indicates that the morphology of the plume conduit has elements consistent with both views: the main anomaly extends down to the bottom of our model in the TZ, but its deep part is not beneath Iceland.

260

In the TZ, we image the plume more than 900 km northwest of Iceland, under eastern Greenland (Fig. 8b,c). *P*-wave tomography studies showed low-velocities beneath eastern Greenland as early as the 1990s[7], interpreting them as one of many branches of the plume, and the same feature can be seen in
265 many recent *P*- and *S*-wave models (Fig. S4). Most *P*-wave models that yield the highest resolution in the NE Atlantic show pronounced low velocities in the TZ under eastern Greenland (Fig. S5), in agreement with NAT2021. Some, although not all, body-wave models also show low velocities in the TZ directly

underneath Iceland. Body-wave models achieve the best resolution at depths
270 sampled by crossing rays. In the upper mantle, they can be strongly biased
by ray-path geometry[13] and station distribution, which is characterized by an
isolated station cluster in Iceland. Seismic stations in eastern Greenland, on
the other hand, are distributed more evenly, especially if recent deployments
are included, so that the low velocities imaged beneath it—in agreement with
275 NAT2021—are not likely to be an artifact caused by ray path geometry.

TZ thickness (dH_{TZ}) is a reliable gauge of the TZ temperature, with thin TZ
indicative of anomalously high temperatures within it[53]. An area of thin TZ
was detected beneath southern Iceland by receiver functions[12] and interpreted
280 as evidence for a plume conduit. More recently, a study using a much larger
regional dataset[54] revealed that the previously detected TZ thinning was one
part in a pattern of small-scale, dH_{TZ} variations around Iceland, changing from
positive to negative over length scales of a few hundred kilometers (Fig. 8b,c).
Interestingly, similar dH_{TZ} variations have been mapped beneath the Hawaii
285 Hotspot[55], suggesting that downwellings of portions of lithospheric mantle
material may occur commonly in the vicinity of an active volcanic hotspot[56].
Beneath Greenland, both NAT2021 and receiver functions[54] display broad,
prominent anomalies indicative of high temperature, with the lowest velocities
and thinnest TZ collocated beneath eastern Greenland. Here, the reported dH_{TZ}
290 is up to 10-12 km lower than global average—depending on the tomographic
model used in converting the differential delay times to the TZ thickness (Fig.
S6, appendix B). We correct the dH_{TZ} anomaly computed in a global-average
seismic velocity model by using the mineralogical Clapeyron slopes of the phase
transformations that give rise to the 410 and 660-km discontinuities[53]. Ap-
295 plying this correction, confirmed by seismic data[53], we estimate an excess
temperature of 120-140° K in the TZ under eastern Greenland. This is consis-
tent with independent petrological estimates for the temperature anomaly in the
asthenosphere beneath Iceland[57]. Overall, the distribution of dH_{TZ} [54] shows
a strong similarity to that of S -wave velocities in the TZ (Fig. 8c). NAT2021 is

300 smoother than the distribution of dH_{TZ} measurements, and shows no anomaly
to a weak positive anomaly close to Iceland, likely reflecting an averaging out
of small-scale positive and negative anomalies evidenced by receiver functions.
Evidence from receiver functions and tomography is thus consistent and indi-
cates that the largest thermal anomaly in the TZ is located beneath eastern
305 Greenland, not beneath Iceland. If a hot (and thus seismically slow) anomaly of
comparable size were present below Iceland, NAT2021 would be able to resolve
it, as confirmed by structural resolution tests (Fig. S7, appendix B).

The downward continuation of the plume anomaly into the lower mantle is
310 beyond the 660-km depth limit of NAT2021, but we can compare our model with
published whole-mantle models (Fig. 9). P- and S-wave whole-mantle models
(Fig. S4) can differ substantially in the region—and S-wave models especially—,
but beneath the Northeast Atlantic they consistently image a low-velocity con-
duit that is strongly tilted in the NW-SE direction (Fig. S5), with a pronounced
315 kink at 1000 km depth that changes the upwelling direction from SE to NW,
pointing towards both Iceland and Greenland in the TZ and upper mantle. In
the shallow lower mantle and TZ, above 1000 km depth, older and smoother
models favour a slightly tilted conduit rising quasi-vertically beneath Iceland, in
agreement with early studies[7, 12] and the vertical plume paradigm. More re-
320 cent and detailed models however show a strong tilt in the conduit, with many
of the low velocities reaching eastern Greenland in the TZ (Fig. S5), where
NAT2021 maps the plume. Interestingly, NAT2021 images a high velocity body
in the deep upper mantle extending from Britain and Ireland to southern Ice-
land within the TZ (Fig. 8b). This anomaly is also seen in most *P*- and *S*-wave
325 models (Figs. 9, S4, S5), with its deepest point sitting directly above the kink
in the plume conduit at 1000 km depth. Its presence and location may indicate
a cold downwelling interfering with the plume, possibly contributing to the ob-
served change in the conduit direction.

330 *3.3. Mantle structure and NAIP magmatism*

In the shallow upper mantle, the plume location imaged by NAT2021 is consistent with the recent volcanism and seamount distribution (Fig. 7). By rotating NAT2021 following plate reconstructions[58], we can explain some of the complexity of the NAIP by comparing the lithospheric structure, the location of the plume stem in the TZ according to NAT2021 and the distribution
335 of volcanism over the past 60 My (Fig. 10). Different plate reconstructions and global hotspot reference frames, however, can yield very different hotspot tracks, and the plume itself may have moved and tilted in time[23]. In NAT2021 we observe that the greatest tilt of the plume’s axis is found in the sub-lithospheric
340 upper mantle, where it interacts with the complex topography of the LAB (Fig. 8b). For this reason, we choose to reconstruct the location of the plume stem in the TZ (identified as the TZ average -1% dVs), beneath this large tilt. While the stem may also have moved in time because of mantle wind, the conduit we image in the TZ is over 300 km in diameter, and fits both static- and moving
345 hotspot tracks within its area (Fig. 10d); we assume its location as static for the purposes of this reconstruction.

At 60 Ma, the plume was beneath the western Rae craton, probably causing the early NAIP volcanism in western Greenland. At 45 Ma, the plume stem was in the middle of the continent, between the North Atlantic and Rae
350 cratons, with the flow of the plume material west and east within the thinner-lithosphere corridor causing the quasi-simultaneous volcanism in western and eastern Greenland[25, 23]. Later, with Greenland slowly moving north-west over the plume, the volcanism in western Greenland waned, the plume material now being deflected east by the continental lithosphere thickness varia-
355 tions. Eventually, volcanism in Greenland mostly ceased as the plume was captured by the spreading ridge, with the only site of recent, post-breakup on-shore magmatism[47] located directly above the plume stem imaged by NAT2021.

The reconstructed positions of both the plume stem and the Iceland Hotspot are far from the location of the British Tertiary Igneous Province (BTIP), also
360 attributed to the Iceland Plume activity[27, 30, 10], which prompts the question

of why the plume could reach the BTIP during the Paleocene but has remained at, and west of, the MAR since then. Before the onset of the seafloor spreading, the thick lithosphere of the Rae and Baltic cratons bordered the thinner continental lithosphere of the Eurasian margin, which likely had only mild variations in thickness, not obstructing and possibly guiding the southeastward flow of the hot asthenosphere from the plume. With the onset of seafloor spreading 56 Myr ago, the strong thinning of the lithosphere along the ridge axis formed a valley that captured the plume material and diverted its flow to north and south along its axis. The plume was then captured by the ridge, and the volcanism of the BTIP waned[25].

4. Conclusion

The uneven distribution of seismic stations in the Northeast Atlantic region has long posed a challenge to tomographic imaging, fuelling decades of debate on the nature and shape of the Iceland Plume. With NAT2021, we collected all available data in the region, including newly available data from Greenland, North America and northwestern Europe, to constrain a new model of the crust and upper mantle beneath it. Compared to previous global and regional models, NAT2021 has a substantially higher resolution, resulting from the unprecedented data coverage and an adaptive regularisation scheme. In Greenland, the model reveals, for the first time, three separate cratonic cores, with the Inglefield-Melville Craton in its northwestern corner separated from the rest of the Rae Craton by a belt of thinner lithosphere. In the shallow upper mantle beneath the Northeast Atlantic Ocean, our model displays in detail the complexity of the low-velocity anomalies beneath the MAR and Iceland. It shows a generally hotter lithosphere west of the ridge, in agreement with the distribution of recent intraplate volcanism. At greater depths, a large low velocity body, located beneath central-eastern Greenland in the transition zone, rises at an angle towards Iceland and the MAR, following the gradient of the lithospheric thickness of the cratons in Greenland and the cooling oceanic lithosphere. The vertical conti-

390 nuity of this prominent anomaly identifies the low-velocity body as the Iceland
Plume.

Our novel view of the plume is in agreement with recent, independently de-
rived data on seamount volcanism and with the evidence from seismic receiver
functions. We suggest that it reconciles the alternative views which, until now,
395 seemed mutually exclusive: the pronounced low-velocity anomaly that we im-
age beneath Iceland itself extends down to 350-400 km depth only, but this is
because the plume conduit tilts to the NNW with increasing depth, reaching
to beneath eastern Greenland in the transition zone. The tomographic images
of the plume, together with the geological and geochemical data on the NAIP
400 magmatism, show how the morphology of the hot mantle upwelling is formed
by its interaction with the thick cratonic lithosphere of Greenland and with the
spreading MAR, which has captured the plume.

Data availability

The tomographic model NAT2021 will be available to download at the main
405 author's website.

Declaration of competing interests

The authors declare that they have no known competing financial interests or
personal relationships that could have appeared to influence the work reported
in this paper.

410 **Acknowledgements**

We thank Charlotte Schoonman, an anonymous reviewer and the Editor,
Rebecca Bendick, for constructive comments and suggestions that helped us to
improve the manuscript. We thank Jennifer Jenkins and Ross Parnell-Turner
for providing the receiver function and dated NAIP volcanism data, respectively.
415 We are grateful to the operators of the seismic networks in Greenland, Iceland

and elsewhere for collecting the seismic data and to the Incorporated Research
Institutions for Seismology (IRIS; <http://www.iris.edu>), the GEOFON Global
Seismic Network (<https://geofon.gfz-potsdam.de>) and Observatories and Re-
search Facilities for European Seismology (<http://www.orfeus-eu.org>) for pro-
420 viding the data used in this study. All figures were implemented with the
Generic Mapping Tools (GMT, <https://www.generic-mapping-tools.org>) and
ParaView (<https://www.paraview.org>). This work was supported by the Sci-
ence Foundation Ireland (SFI) grant 13/CDA/2192, SFI grant 16/IA/4598, co-
funded by the Geological Survey of Ireland and the Marine Institute, and SFI
425 grant 13/RC/2092, co-funded under the European Regional Development Fund.
This work has been completed in the framework of the project 3D Earth funded
by the European Space Agency (ESA) as a Support to Science Element (STSE).
CG acknowledges support from the Research Council of Norway, through its
Centre of Excellence scheme, project number 223272 (CEED).

430 **Appendix A. Adaptive regularization**

The linear inversion is regularized by lateral and vertical smoothing and
a slight norm damping. Typically, a single coefficient determines the amount
of norm damping or smoothing applied for each parameter, which will affect
variously sampled nodes differently. A choice of norm damping suitable for
435 imaging a well-sampled lithosphere will result in overdamping of deeper, less
sampled nodes, lowering the amplitudes of the anomalies; conversely, the less
sampled—and thus more susceptible to errors—greater depths would benefit
from more smoothing, undesired in the well sampled lithosphere. This issue
is prominent in global tomographic imaging due to the very strong lateral and
440 vertical variations in sampling (Fig. 2).

In order to account differently sampled nodes, we scale regularization with data
sampling in three-dimensions (3D). This is implemented by scaling the norm
damping and lateral smoothing coefficients with the sums of the columns of
the sensitivity matrix. Column sums are quantities that contain information

445 on the number of sensitivity areas sampling the node, the sensitivity kernel weights and the path-similarity weights[36], making them good indicators of data sensitivity. We scale norm damping proportionally to the column sums, while lateral smoothing is scaled inversely. This way, well sampled nodes will be more damped and less smoothed while poorly sampled ones will be less damped
450 but smoothed more. The regularization coefficients for both lateral smoothing and norm damping are separately scaled vertically and horizontally :

$$f(i, j) = f_0 * f_{sV}(j) * f_{sH}(i, j); \quad (1)$$

$$f_{sV}(j) = \frac{cs_{ave(j)}/cs_{max} + \epsilon_V}{\epsilon_V + 1}, \quad f_{sH}(i, j) = \frac{cs(i, j)/cs_{max(j) + \epsilon_H}}{\epsilon_H + 1}; \quad (2)$$

where $f(i, j)$ is the regularization factor for the i -th node of the model grid at the j -th depth layer. f_0 is the initial, unscaled regularization factor, $f_{sV}(j)$
455 and $f_{sH}(i, j)$ the vertical and horizontal scaling and $cs(i, j)$ the column sums. Vertical scaling $f_{sV}(j)$ takes into account the change of the column sums across depth layers, and is based on their j -th depth layer average $cs_{ave(j)}$, normalized to the global maximum cs_{max} . Horizontal scaling $f_{sH}(i, j)$ includes the lateral variations of column sums at each i -th point within each j -th layer, normalized
460 to the layer maximum $cs_{max(j)}$. The ϵ values determine how much each scaling is effective, and are chosen empirically. For $\epsilon = 0$, the scaling factor is equal to the normalized column sums, yielding the largest scaling. Increasing ϵ will progressively reduce the effect of the column sum scaling in a non-linear way (Fig. S1).

465 While our intention is to make the regularization take sampling into account, it is advisable to choose non-zero ϵ values for norm-damp scaling to tame the effect of data errors and inconsistencies in the model. For smoothing scaling, the same rule applies to prevent over-smoothing of greater depths and least sampled areas resulting from the very large values of $1/f_s$ (Fig. S1).

470 The effects of different ϵ values for both vertical and horizontal scaling are shown in Fig. S2 at 56, 150 and 485 km depth. Scaling factor values are normalized to the global average to highlight the variance. Lower ϵ values allow for greater variation in the scaling factor, while higher values produce almost no scaling.

For low ϵ_V and high ϵ_H , little scaling is visible for each depth layer, but the coefficients change noticeably across depths. For high ϵ_V and low ϵ_H , we observe strong lateral changes, while the coefficients vary only mildly with depth, due to the average vertical variations of the column sums.

For our final model, we chose mild vertical- and strong lateral scaling values for both norm damping and lateral smoothing (Fig. S1). The choice of a mild vertical scaling is to both avoid underregularization of deeper, less constrained depths, and to account for the vertical changes inherently present within the horizontal scaling (i.e. there are less areas of highly sampled nodes at great depths). Additionally, we introduce a layer-average manual scaling (Fig. S2d, h): for norm damping, we reduce the coefficients at the discontinuities, to account for the presence of adjacent node layers; for lateral smoothing, we increase the coefficients at shallow depths, to smooth high-frequency oscillations.

Appendix B. Supplementary material

References

- [1] A. D. Saunders, J. G. Fitton, A. C. Kerr, M. J. Norry, R. W. Kent, The north atlantic igneous province, Large Igneous Provinces: Continental, Oceanic, and Planetary Flood Volcanism (JANUARY) (1997) 45–93. doi:10.1029/GM100p0045.
- [2] W. J. Morgan, Convection Plumes in the Lower Mantle, Nature 230 (1971) 42–43.
- [3] J.-G. Schilling, Iceland Mantle Plume: Geochemical Study of Reykjanes Ridge, Nature 242 (1973) 565–571.
- [4] S. Goes, F. Cammarano, U. Hansen, Synthetic seismic signature of thermal mantle plumes, Earth and Planetary Science Letters 218 (3-4) (2004) 403–419. doi:10.1016/S0012-821X(03)00680-0.
- [5] C. J. Wolfe, I. T. Bjarnason, J. C. VanDecar, S. C. Solomon, Seismic structure of the Iceland mantle plume, Letters to Nature 385 (1997) 245–247.

- [6] J. Ritsema, H. J. Van Heijst, J. H. Woodhouse, Complex shear velocity structure imaged beneath Africa and Iceland, *Science* 286 (DECEMBER) (1999) 1925–1928. doi:10.1126/science.286.5446.1925.
- 505 [7] H. Bijwaard, W. Spakman, Tomographic evidence for a narrow whole mantle plume below Iceland, *Earth and Planetary Science Letters* 166 (3-4) (1999) 121–126. doi:10.1016/S0012-821X(99)00004-7.
- [8] R. M. Allen, G. Nolet, J. P. Morgan, K. Vogfjörð, B. H. Bergsson, P. Erlendsson, Imaging the mantle beneath Iceland using integrated seismological techniques, *Journal of Geophysical Research* 107 (B12) (2002) ESE 3
510 1—16. doi:10.1029/2001JB000595.
- [9] S. Pilidou, K. Priestley, E. Debayle, Ó. Gudmundsson, Rayleigh wave tomography in the North Atlantic: High resolution images of the Iceland, Azores and Eifel mantle plumes, *Lithos* 79 (3-4 SPEC. ISS.) (2005) 453–
515 474. doi:10.1016/j.lithos.2004.09.012.
- [10] F. Rickers, A. Fichtner, J. Trampert, The Iceland-Jan Mayen plume system and its impact on mantle dynamics in the North Atlantic region: Evidence from full-waveform inversion, *Earth and Planetary Science Letters* 367 (2013) 39–51. doi:10.1016/j.epsl.2013.02.022.
- 520 [11] G. R. Foulger, D. G. Pearson, Is Iceland underlain by a plume in the lower mantle? Seismology and helium isotopes, *Geophysical Journal International* 145 (2001) F1–F5. doi:10.1046/j.0956-540x.2001.01457.x.
- [12] Y. Shen, S. C. Solomon, I. T. Bjarnason, G. Nolet, W. J. Morgan, R. M. Allen, K. Vogfjörð, S. Jakobsdóttir, R. Stefánsson, B. R. Julian, G. R.
525 Foulger, Seismic evidence for a tilted mantle plume and north-south mantle flow beneath Iceland, *Earth and Planetary Science Letters* 197 (3-4) (2002) 261–272. doi:10.1016/S0012-821X(02)00494-6.
- [13] W. R. Keller, D. L. Anderson, R. W. Clayton, Resolution of tomographic

- models of the mantle beneath Iceland, *Geophysical Research Letters* 27 (24)
530 (2000) 3993–3996. doi:10.1029/2000GL011798.
- [14] G. R. Foulger, Plumes, or plate tectonic processes?, *Astronomy & Geophysics* 43 (6) (2002) 6.19–6.23. doi:10.1046/j.1468-4004.2002.43619.x.
- [15] A. L. Peace, J. Phethean, D. Franke, G. Foulger, C. Schiffer, J. Welford,
535 G. McHone, S. Rocchi, M. Schnabel, A. Doré, A review of Pangaea dispersal and Large Igneous Provinces In search of a causative mechanism, *Earth-Science Reviews* 206 (March 2019) (2020) 102902. doi:10.1016/j.earscirev.2019.102902.
- [16] S. W. French, B. Romanowicz, Broad plumes rooted at the base of the
540 Earth’s mantle beneath major hotspots, *Nature* 525 (7567) (2015) 95–99. doi:10.1038/nature14876.
- [17] P. Glišović, A. M. Forte, Two deep-mantle sources for Paleocene doming and volcanism in the North Atlantic, *Proceedings of the National Academy of Sciences* (2019) 1–6doi:10.1073/pnas.1816188116.
- 545 [18] I. T. Bjarnason, H. Schmeling, The lithosphere and asthenosphere of the Iceland hotspot from surface waves, *Geophysical Journal International* 178 (1) (2009) 394–418. doi:10.1111/j.1365-246X.2009.04155.x.
- [19] T. H. Torsvik, H. E. F. Amundsen, R. G. Trønnes, P. V. Doubrovine, C. Gaina, N. J. Kuszniir, B. Steinberger, F. Corfu, L. D. Ashwal, W. L.
550 Griffin, S. C. Werner, B. Jamtveit, Continental crust beneath southeast Iceland., *Proceedings of the National Academy of Sciences* 112 (15) (2015) E1818–27. doi:10.1073/pnas.1423099112.
- [20] M. J. Hoggard, N. White, D. Al-Attar, Global dynamic topography observations reveal limited influence of large-scale mantle flow, *Nature Geoscience* 9 (6) (2016) 456–463. doi:10.1038/ngeo2709.
555

- [21] J. Fitton, A. Saunders, M. Norry, B. Hardarson, R. Taylor, Thermal and chemical structure of the Iceland plume, *Earth and Planetary Science Letters* 153 (3-4) (1997) 197–208. doi:10.1016/S0012-821X(97)00170-2.
- [22] J. Korenaga, P. B. Kelemen, Major element heterogeneity in the mantle source of the North Atlantic igneous province, *Earth and Planetary Science Letters* 184 (1) (2000) 251–268. doi:10.1016/S0012-821X(00)00308-3.
- [23] B. Steinberger, E. Bredow, S. Lebedev, A. Schaeffer, T. H. Torsvik, Widespread volcanism in the Greenland-North Atlantic region explained by the Iceland plume, *Nature Geoscience* 12 (2019) 61–68. doi:10.1038/s41561-018-0251-0.
- [24] M. Ganerød, M. A. Smethurst, T. H. Torsvik, T. Prestvik, S. Rousse, C. McKenna, D. J. van Hinsbergen, B. W. Hendriks, The North Atlantic Igneous Province reconstructed and its relation to the Plume Generation Zone: The Antrim Lava Group revisited, *Geophysical Journal International* 182 (1) (2010) 183–202. doi:10.1111/j.1365-246X.2010.04620.x.
- [25] C. M. Wilkinson, M. Ganerød, B. W. H. Hendriks, E. A. Eide, Compilation and appraisal of geochronological data from the North Atlantic Igneous Province (NAIP), Geological Society, London, Special Publications 447 (1) (2016) 69–103. doi:10.1144/SP447.10.
- [26] P. Japsen, J. A. Chalmers, Neogene uplift and tectonics around the North Atlantic: Overview, *Global and Planetary Change* 24 (3-4) (2000) 165–173. doi:10.1016/S0921-8181(00)00006-0.
- [27] N. White, B. Lovell, Measuring the pulse of a plume with the sedimentary record, *Nature* 387 (6636) (1997) 888–891. doi:10.1038/43151.
- [28] C. M. Schoonman, N. White, D. Pritchard, Radial viscous fingering of hot asthenosphere within the Icelandic plume beneath the North Atlantic Ocean, *Earth and Planetary Science Letters* 468 (2017) 51–61. doi:10.1016/j.epsl.2017.03.036.

- [29] M. L. Amaru, Global travel time tomography with 3-D reference models, Ph.D. thesis, Utrecht University (2007).
585
- [30] S. J. Arrowsmith, M. Kendall, N. White, J. C. VanDecar, D. C. Booth, Seismic imaging of a hot upwelling beneath the British Isles, *Geology* 33 (5) (2005) 345–348. doi:10.1130/G21209.1.
- [31] C. Gaina, A. Blischke, W. H. Geissler, G. S. Kimbell, O. G. Erlendsson, Seamounts and oceanic igneous features in the NE Atlantic: A link between
590 plate motions and mantle dynamics, *Geological Society Special Publication* 447 (1) (2017) 419–442. doi:10.1144/SP447.6.
- [32] S. Lebedev, G. Nolet, T. Meier, R. D. van der Hilst, Automated multimode inversion of surface and S waveforms, *Geophysical Journal International*
595 162 (3) (2005) 951–964. doi:10.1111/j.1365-246X.2005.02708.x.
- [33] G. Ekström, M. Nettles, A. M. Dziewonski, The global CMT project 2004-2010: Centroid-moment tensors for 13,017 earthquakes, *Physics of the Earth and Planetary Interiors* 200-201 (2012) 1–9. doi:10.1016/j.pepi.2012.04.002.
- [34] A. J. Schaeffer, S. Lebedev, Global shear speed structure of the upper mantle and transition zone, *Geophysical Journal International* 194 (1) (2013) 417–449. doi:10.1093/gji/ggt095.
600
- [35] G. Nolet, Partitioned Waveform Inversion and two-dimensional structure under the network of autonomously recording seismographs, *Journal of Geophysical Research* 95 (89) (1990) 8499. doi:10.1029/JB095iB06p08499.
605
- [36] S. Lebedev, R. D. van der Hilst, Global upper-mantle tomography with the automated multimode inversion of surface and S-wave forms, *Geophysical Journal International* 173 (2) (2008) 505–518. doi:10.1111/j.1365-246X.2008.03721.x.
610

- [37] C. C. Paige, M. A. Saunders, LSQR: An Algorithm for Sparse Linear Equations and Sparse Least Squares, *ACM Transactions on Mathematical Software* 8 (1) (1982) 43–71. doi:10.1145/355984.355989.
- [38] Z. Wang, F. A. Dahlen, Spherical-spline parameterization of three-dimensional Earth models, *Geophysical Research Letters* 22 (22) (1995) 3099–3102.
- [39] C. Bassin, G. Laske, G. Masters, The Current Limits of Resolution for Surface Wave Tomography in North America, *EOS Trans AGU* 81 (2000) F897.
- [40] C. P. Legendre, T. Meier, S. Lebedev, W. Friederich, L. Viereck-Götte, A shear wave velocity model of the European upper mantle from automated inversion of seismic shear and surface waveforms, *Geophysical Journal International* 191 (1) (2012) 282–304. doi:10.1111/j.1365-246X.2012.05613.x.
- [41] N. L. Celli, S. Lebedev, A. J. Schaeffer, M. Ravenna, C. Gaina, The upper mantle beneath the South Atlantic Ocean, South America and Africa from waveform tomography with massive data sets, *Geophysical Journal International* 221 (2020) 178–204. doi:10.1093/gji/ggz574.
- [42] S. Lebedev, A. J. Schaeffer, J. Fulla, V. Pease, M. Square, Seismic tomography of the Arctic region: inferences for the thermal structure and evolution of the lithosphere, in: V. Pease, B. Coakley (Eds.), *Circum-Arctic Lithosphere Evolution*, Geological Society of London Special Publication, 2018. doi:https://doi.org/10.1144/SP460.10.
- [43] S. W. French, V. Lekic, B. Romanowicz, Waveform tomography reveals channeled flow at the base of the oceanic asthenosphere., *Science* 342 (6155) (2013) 227–30. doi:10.1126/science.1241514.
- [44] E. Debayle, F. Dubuffet, S. Durand, An automatically updated S - wave model of the upper mantle and the depth extent of azimuthal

- anisotropy, *Geophysical Research Letters* 43 (2) (2016) 674–682. doi:
640 10.1002/2015GL067329.
- [45] Y. Niu, R. Hékinian, Spreading-rate dependence of the extent of mantle melting beneath ocean ridges, *Nature* 385 (6614) (1997) 326–328. doi: 10.1038/385326a0.
- [46] J. A. Chalmers, T. C. Pulvertaft, Development of the continental margins of the Labrador Sea: A review, *Geological Society Special Publication* 187
645 (2001) 77–105. doi:10.1144/GSL.SP.2001.187.01.05.
- [47] M. Storey, A. K. Pedersen, O. Stecher, S. Bernstein, H. C. Larsen, L. M. Larsen, J. A. Baker, R. A. Duncan, Long-lived postbreakup magmatism along the East Greenland margin: Evidence for shallow-mantle metasomatism by the Iceland plume, *Geology* 32 (2) (2004) 173–176. doi:
650 10.1130/G19889.1.
- [48] N. L. Celli, S. Lebedev, A. J. Schaeffer, C. Gaina, African cratonic lithosphere carved by mantle plumes, *Nature Communications* 11 (1) (2020) 92. doi:10.1038/s41467-019-13871-2.
- 655 [49] W. J. Morgan, Rodriguez, Darwin, Amsterdam, a second type of hotspot island, *Journal of Geophysical Research* 83 (B11) (1978) 5355–5360.
- [50] J.-P. Montagner, J. Ritsema, Interactions between Ridges and Plumes, *Science* 294 (5546) (2001) 1472–1473.
- [51] N. H. Sleep, Lateral flow and ponding of starting plume material, *Journal of Geophysical Research-Solid Earth* 102 (B5) (1997) 10001–10012. doi:
660 10.1029/97jb00551.
- [52] J. M. Whittaker, J. C. Afonso, S. Masterton, R. D. Müller, P. Wessel, S. E. Williams, M. Seton, Long-term interaction between mid-ocean ridges and mantle plumes, *Nature Geoscience* 8 (6) (2015) 479–484. doi:10.1038/
665 NGE02437.

- [53] S. Lebedev, G. Nolet, Upper mantle beneath Southeast Asia from S velocity tomography, *J. Geophys. Res.* 108 (B1) (2003) 2048. doi:10.1029/2000jb000073.
- [54] J. Jenkins, S. Cottaar, R. S. White, A. Deuss, Depressed mantle discontinuities beneath Iceland: Evidence of a garnet controlled 660 km discontinuity?, *Earth and Planetary Science Letters* 433 (2016) 159–168. doi:10.1016/j.epsl.2015.10.053.
URL <http://dx.doi.org/10.1016/j.epsl.2015.10.053>
- [55] M. R. Agius, C. A. Rychert, N. Harmon, G. Laske, Mapping the mantle transition zone beneath Hawaii from Ps receiver functions: Evidence for a hot plume and cold mantle downwellings, *Earth and Planetary Science Letters* 474 (2017) 226–236. doi:10.1016/j.epsl.2017.06.033.
URL <http://dx.doi.org/10.1016/j.epsl.2017.06.033>
- [56] E. Burov, L. Guillou-Frottier, The plume head-continental lithosphere interaction using a tectonically realistic formulation for the lithosphere, *Geophysical Journal International* 161 (2) (2005) 469–490. doi:10.1111/j.1365-246X.2005.02588.x.
- [57] C. Herzberg, P. D. Asimow, Petrology of some oceanic island basalts: PRIMELT2.XLS software for primary magma calculation, *Geochemistry, Geophysics, Geosystems* 9 (9) (2008) Q09001. doi:10.1029/2008GC002057.
- [58] T. H. Torsvik, B. Steinberger, G. E. Shephard, P. V. Doubrovine, C. Gaina, M. Domeier, C. P. Conrad, W. W. Sager, Pacific-Panthalassic Reconstructions: Overview, Errata and the Way Forward, *Geochemistry, Geophysics, Geosystems* 20 (7) (2019) 3659–3689. doi:10.1029/2019GC008402.
- [59] S. Whitmeyer, K. E. Karlstrom, Tectonic model for the Proterozoic growth of North America, *Geosphere* 3 (4) (2007) 220–259. doi:10.1130/GES00055.1.

- [60] S. V. Bogdanova, B. Bingen, R. Gorbatshev, T. N. Kheraskova, V. I. Kozlov, V. N. Puchkov, Y. A. Volozh, The East European Craton (Baltica) before and during the assembly of Rodinia, *Precambrian Research* 160 (1-2) (2008) 23–45. doi:10.1016/j.precamres.2007.04.024.
- [61] P. Kumar, R. Kind, K. Priestley, T. Dahl-Jensen, Crustal structure of Iceland and Greenland from receiver function studies, *Journal of Geophysical Research: Solid Earth* 112 (3) (2007) 1–19. doi:10.1029/2005JB003991.
- [62] P. R. Dawes, Precambrian - Palaeozoic geology of Smith Sound, Canada and Greenland: Key constraint to palaeogeographic reconstructions of northern Laurentia and the North Atlantic region, *Terra Nova* 21 (1) (2009) 1–13. doi:10.1111/j.1365-3121.2008.00845.x.
- [63] J. Grocott, K. J. McCaffrey, Basin evolution and destruction in an early proterozoic continental margin: The rinkian fold-thrust belt of central west greenland, *Journal of the Geological Society* 174 (3) (2017) 453–467. doi:10.1144/jgs2016-109.
- [64] J. Horni, J. R. Hopper, A. Blischke, W. H. Geissler, M. Stewart, K. McDermott, M. Judge, Ö. Erlendsson, U. Arting, Regional distribution of volcanism within the North Atlantic Igneous Province, Geological Society, London, *Special Publications* 447 (1) (2017) 105–125. doi:10.1144/sp447.18.
- [65] R. Parnell-Turner, N. White, T. J. Henstock, S. M. Jones, J. MacLennan, B. J. Murton, Causes and Consequences of Diachronous V-Shaped Ridges in the North Atlantic Ocean, *Journal of Geophysical Research: Solid Earth* 122 (11) (2017) 8675–8708. doi:10.1002/2017JB014225.
- [66] L. Johansson, S. Zahirovic, R. D. Müller, The Interplay Between the Eruption and Weathering of Large Igneous Provinces and the Deep-Time Carbon Cycle, *Geophysical Research Letters* 45 (11) (2018) 5380–5389. doi:10.1029/2017GL076691.

- [67] A. Fichtner, D. P. vanHerwaarden, M. Afanasiev, S. Simut, L. Krischer, Y. Çubuk-Sabuncu, T. Taymaz, L. Colli, E. Saygin, A. Villaseñor, J. Trampert, P. Cupillard, H. P. Bunge, H. Igel, The Collaborative Seismic Earth Model: Generation 1, *Geophysical Research Letters* 45 (9) (2018) 4007–4016. doi:10.1029/2018GL077338.
- 725
- [68] J. Ritsema, A. Deuss, H. J. Van Heijst, J. H. Woodhouse, S40RTS: A degree-40 shear-velocity model for the mantle from new Rayleigh wave dispersion, teleseismic traveltime and normal-mode splitting function measurements, *Geophysical Journal International* 184 (3) (2011) 1223–1236. doi:10.1111/j.1365-246X.2010.04884.x.
- 730
- [69] C. Lu, S. P. Grand, H. Lai, E. J. Garnero, TX2019slab: A New P and S Tomography Model Incorporating Subducting Slabs, *Journal of Geophysical Research: Solid Earth* 124 (11) (2019) 11549–11567. doi:10.1029/2019JB017448.
- 735
- [70] B. L. N. Kennett, E. R. Engdahl, R. Buland, Constraints on seismic velocities in the Earth from traveltimes, *Geophysical Journal International* 122 (1995) 108–124.
- [71] P. V. Doubrovine, B. Steinberger, T. H. Torsvik, Absolute plate motions in a reference frame defined by moving hot spots in the Pacific, Atlantic, and Indian oceans, *Journal of Geophysical Research: Solid Earth* 117 (9) (2012) 1–30. doi:10.1029/2011JB009072.
- 740

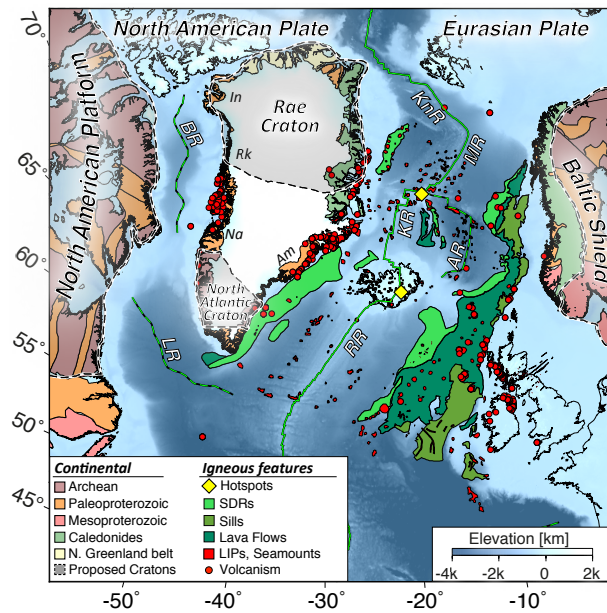


Figure 1: **Simplified tectonic map of the Northeast Atlantic region.** A compilation of continental bedrock geology[59, 60, 61, 62, 63] (colored by age) and igneous features (colored by type and facies) is plotted on top of topography. Submerged volcanic facies[64] are shown in green colors (SDRs: seaward-dipping reflectors). Other igneous features are shown in red: circles are on-shore volcanism[65]; polygons are SOIFs[31] and LIPs[66]. Hotspots are shown as yellow diamonds, past (dashed) and present (solid) mid-ocean ridges are plotted in green: AR, Aegir; BR, Baffin Bay; KR, Kolbeinsey; KnR, Knipovich; LR, Labrador; MR, Mohns; RR, Reykjanes. Mobile belts: Am, Ammassalik; In, Inglefield-Melville; Na, Nagssugtoqidian; Rk, Rinkian.

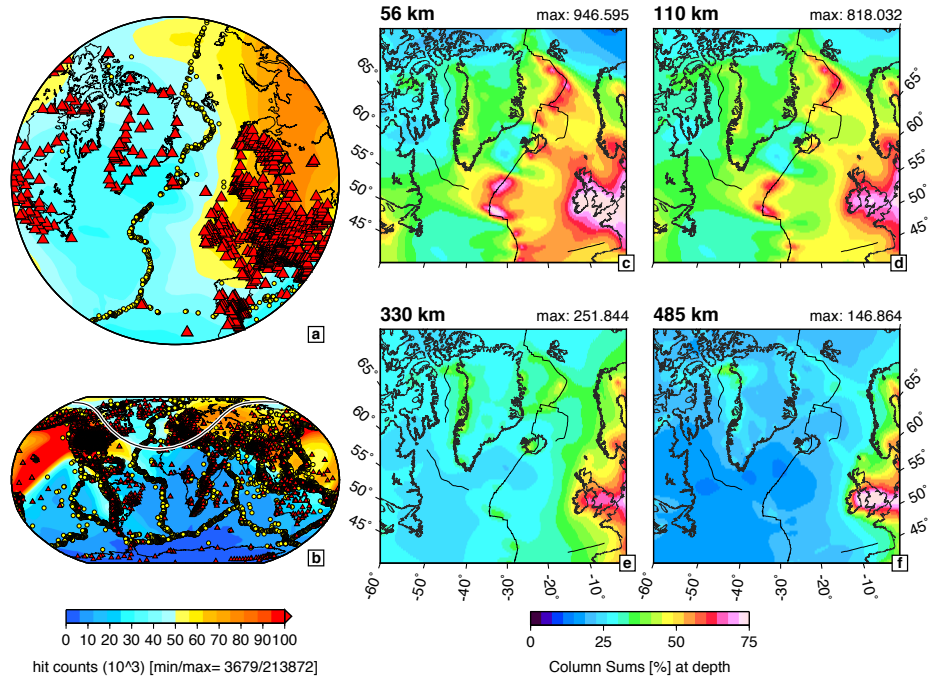


Figure 2: **Data coverage for the NAT2021 tomographic model.** a,b) number of approximate sensitivity areas sampling each node both in the study region and globally. The location of the study area on the globe is shown as black and white lines. The shape—and thus the counting—of the sensitivity areas is depth-invariant. Stations are shown as red triangles, events as yellow circles. c-f) model sensitivity for NAT2021 at 56, 110, 330 and 485 km depth. The sensitivity is represented by the sums of the columns of the sensitivity matrix (see appendix A), in percentage from the max at depth (indicated on the top right corner). In all panels past and present-day plate boundaries area shown in black.

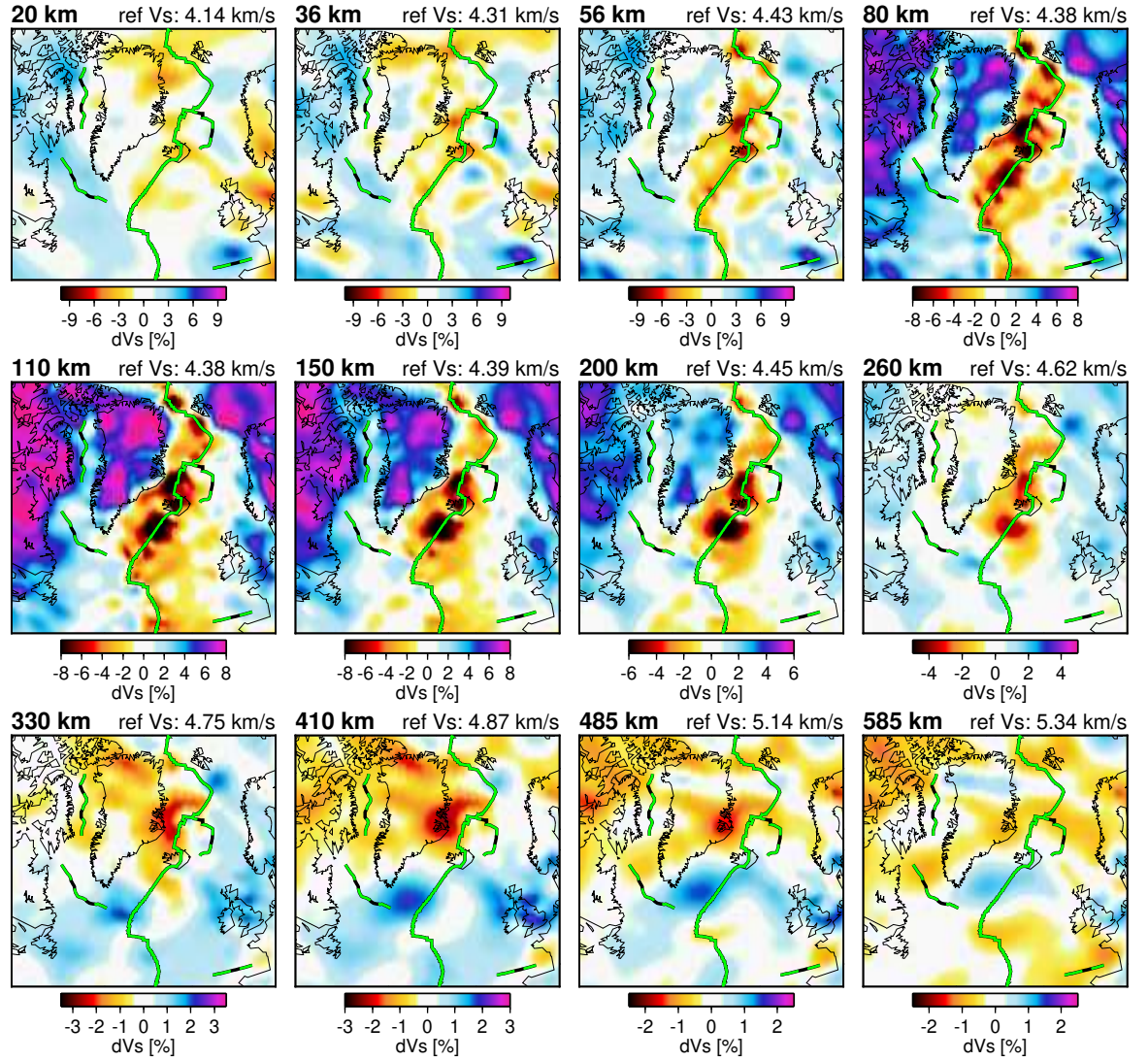


Figure 3: **Horizontal slices through NAT2021.** *S*-wave velocity anomalies, in % from the reference, are shown at 20, 36, 56, 80, 110, 150, 200, 260, 330, 410, 485, 585 km depth. Depth is shown on the top left of each panel, reference velocity in the mantle on the top right. In the crust, the reference is the modified[36] CRUST 2.0[39]. Past (dashed) and present (solid) plate boundaries are plotted in green.

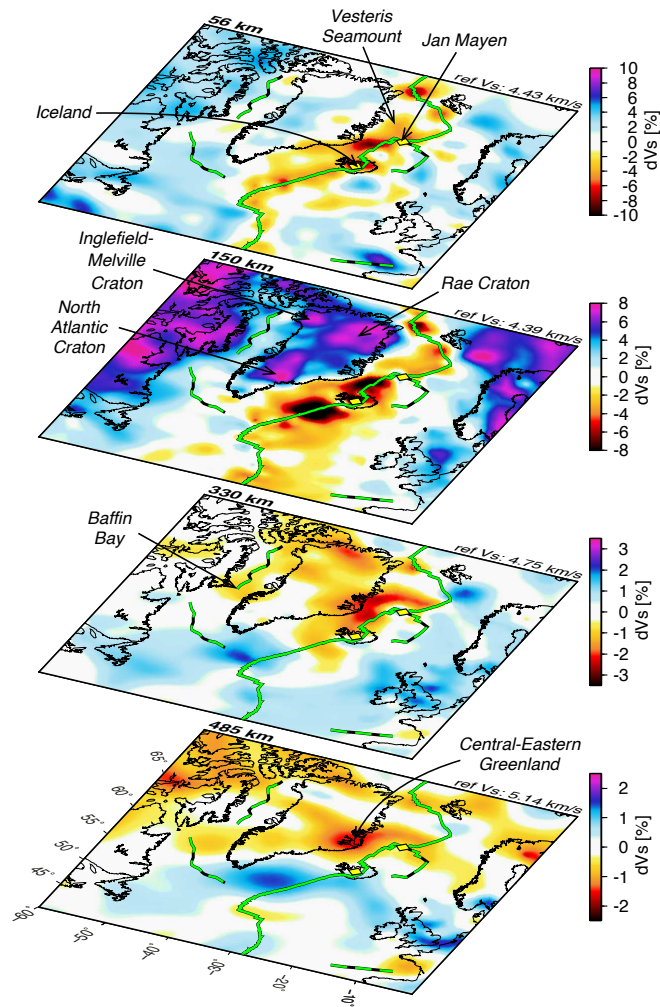


Figure 4: **Depth slices through NAT2021 at 56, 150, 330 and 485 km depths in perspective view.** Depth is shown on the top left of each panel, reference velocity on the top right. Hotspots are shown as yellow diamonds, past (dashed) and present (solid) plate boundaries are plotted in green.

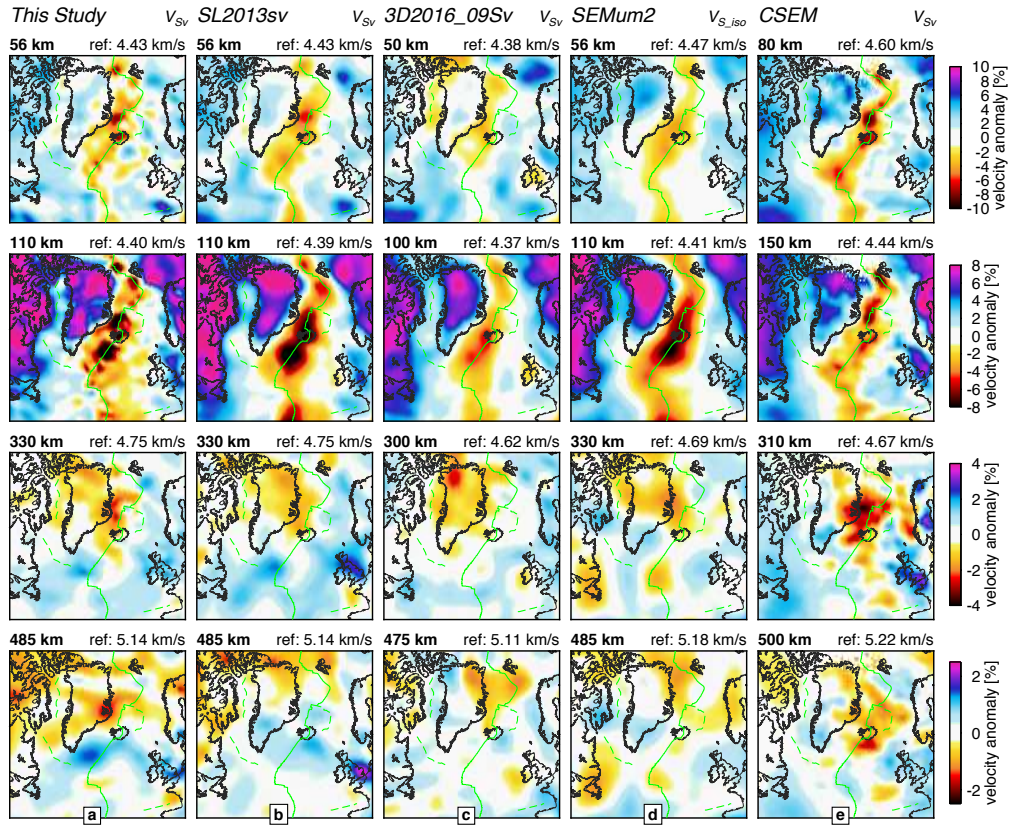


Figure 5: **Comparison of waveform tomography models in the NE Atlantic.** a) NAT2021; b) SL2013sv[34], c) 3D2016Sv[44], d) SEMum2[43], e) CSEM[67], which in this region directly includes[10]. Each model is plotted at the depth node closest to 50, 100, 300 and 485 km depth. Velocity anomalies are computed with respect to the global average at depth. Reference velocity is plotted on the top right of each panel. Past (dashed) and present (continuous) plate boundaries are plotted in green.

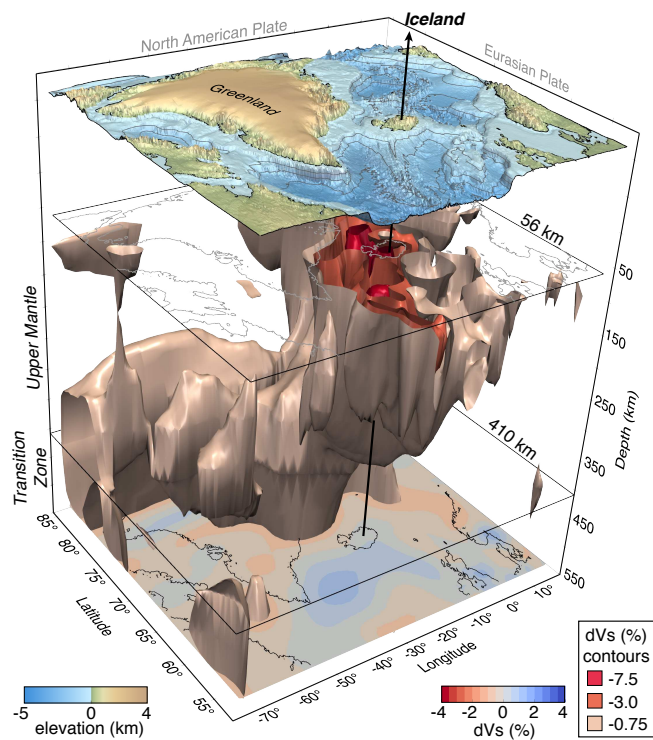


Figure 6: **3D plot of the Iceland Plume as imaged by NAT2021.** The plume is shown using -0.75, -3 and -7.5% velocity anomaly contours between 56 and 550 km depth. Topography is shown on top, with isopachs every km depth. The plot is underlain by the depth slice at 550 km depth. Black outlines mark the 56 km depth and the 410 km discontinuity. Iceland is marked by the vertical black arrow.

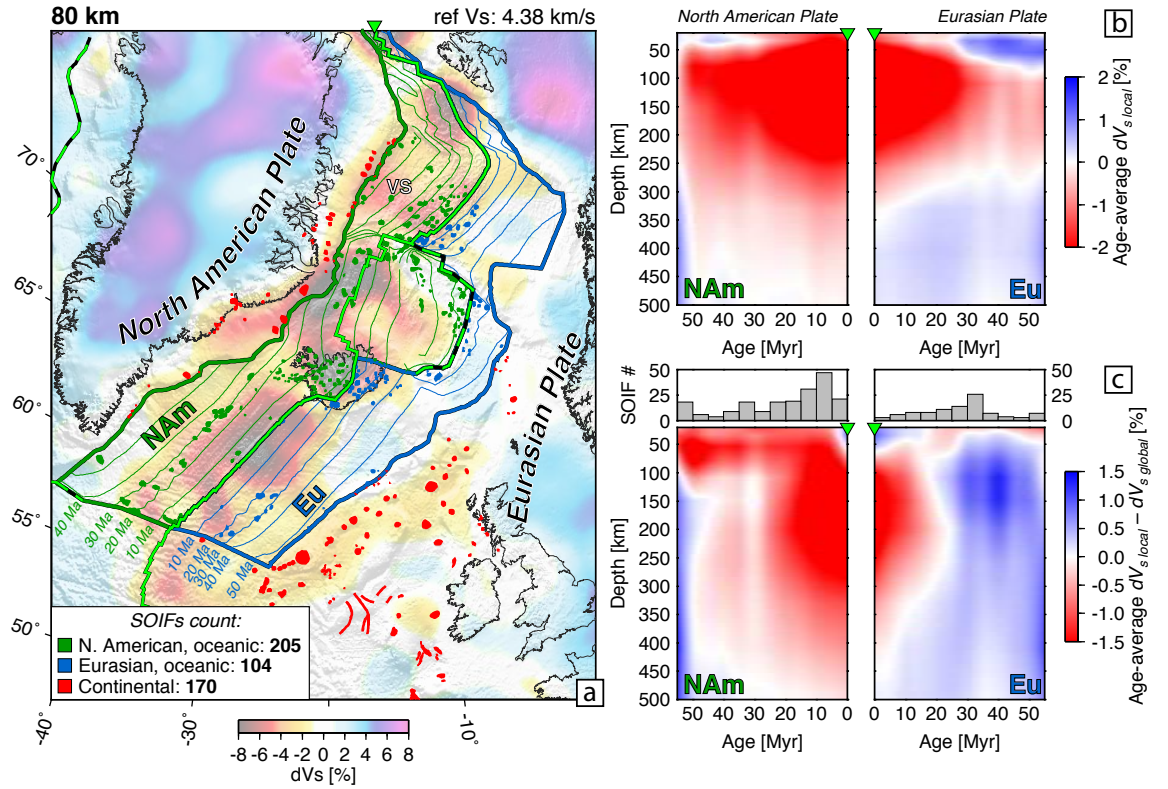


Figure 7: **East-West asymmetry of the mantle structure and volcanism in the Northeast Atlantic.** a) mapview of NAT2021 at 80 km depth. The boundaries of the NE Atlantic oceanic portions of the North American Plate (NAM) and Eurasian Plate (Eu) are plotted in dark green and blue, respectively, with lithospheric age contours every 10 Myr. Past (dashed) and present (solid) plate boundaries are plotted in green. Oceanic SOIFs[31] are colored based on the plate they are located on. Other, continental SOIFs are plotted in red. VS: Vesteris Seamount. b) age-average S -wave velocity anomaly under the oceanic portions of the North American and Eurasian Plates, within the boundaries shown on the map. c) difference between the local- and global age-averages (Fig. S3), with histograms of the distribution of SOIFs on the oceanic lithosphere of different ages on top. In all panels, green inverted triangles mark the location of the MAR at plot boundaries.

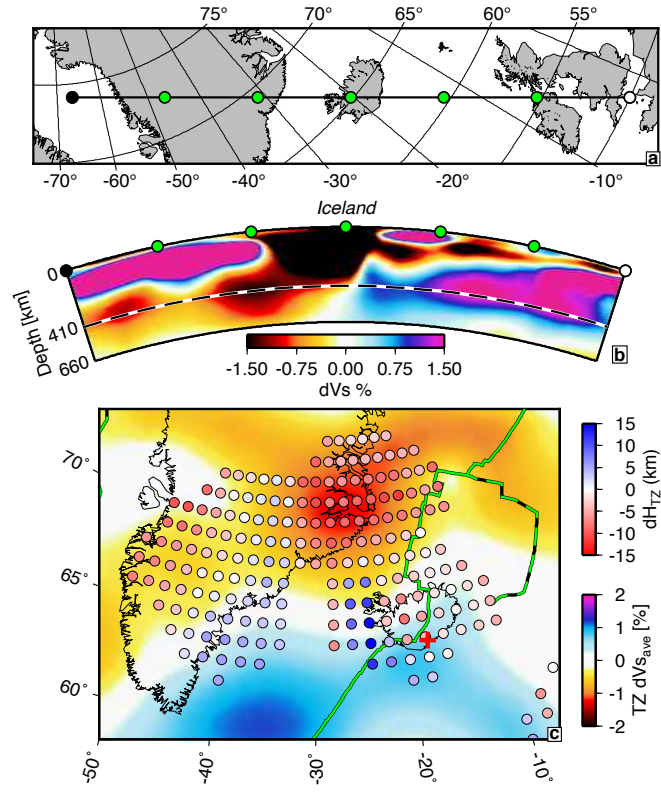


Figure 8: **Upper mantle and transition zone beneath Iceland and Greenland.** a) map of the cross-section. b) cross-section through the Iceland Plume anomaly in NAT2021. The 410 km discontinuity is marked with a dashed black line. c) average S -wave velocity anomaly in the transition zone (410-660 km depth range) from NAT2021, with TZ thickness variations from receiver functions[54], smoothed (Fig. S6) and superimposed as colored circles. The location of thinnest TZ from[12] is shown with a red cross. Past (dashed) and present (solid) plate boundaries are plotted in green.

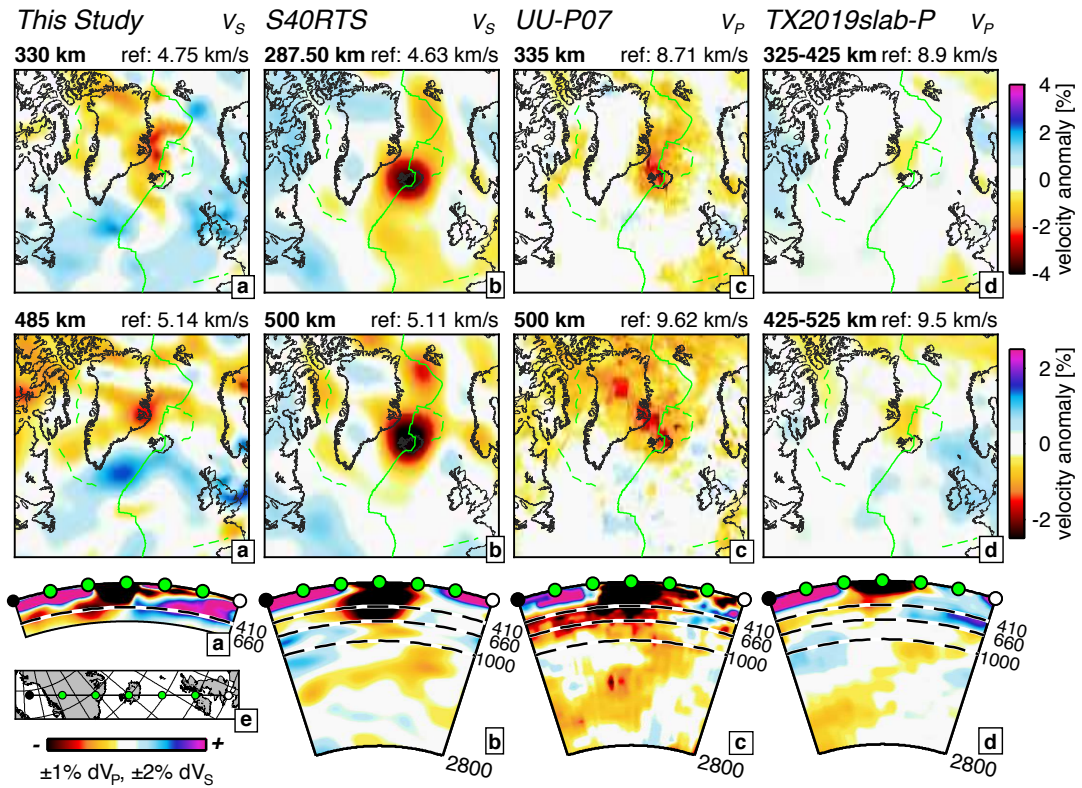


Figure 9: **Comparison of NAT2021 to whole-mantle tomographic models in the NE Atlantic.** a) NAT2021; b) S40RTS[68], c) UU-P07[29] and d) TX2019slab-P[69]. Each model is plotted at the depth node closest to 300 and 485 km depth and in a NW-SE vertical cross-section, mapped in panel e). Velocity anomalies are computed with respect to the global average at depth for V_S and with respect to AK135[70] for V_P . The saturation of the colormap used in the vertical cross-sections is different for V_S and V_P and is indicated in the bottom left color scale. The model type (P - or S -wave) is indicated on the top right of each column. Reference velocity is plotted on the top right of each panel. Past (dashed) and present (continuous) plate boundaries are plotted in green.

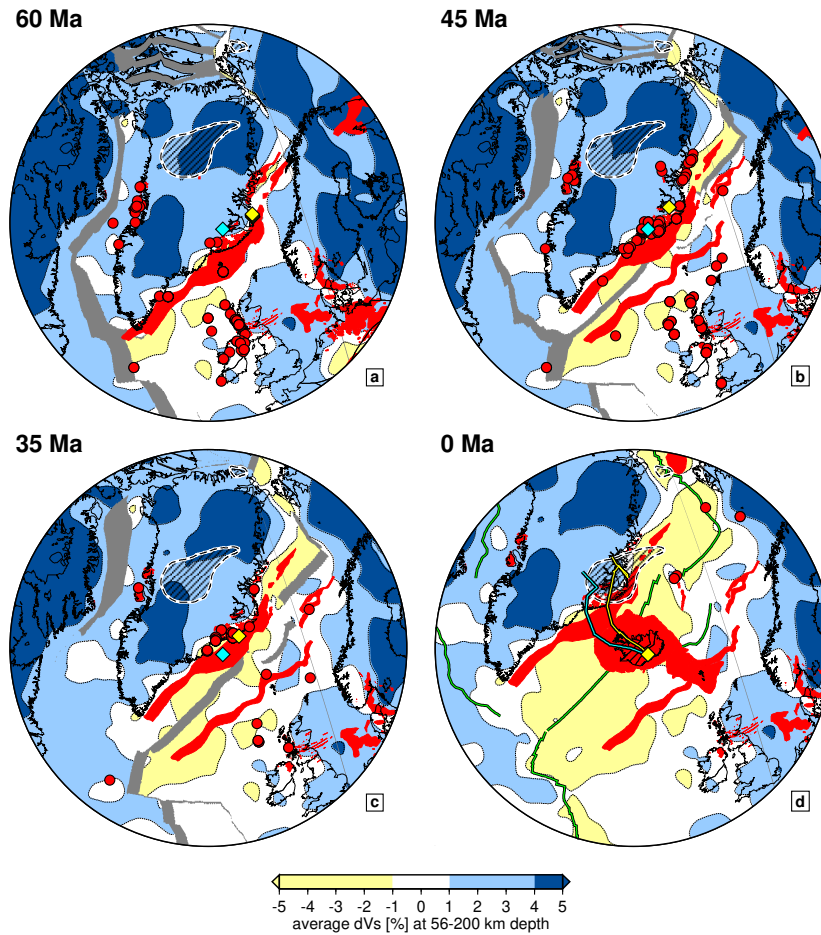


Figure 10: **Lithospheric structure, plate positions, volcanism and hotspot locations in a mantle reference frame at 60, 45, 35 and 0 Ma.** Present-day structure of the lithosphere is assumed at all ages, regionalized using the 56-200 km depth average dVs from NAT2021. Dark blue indicates the coldest, thickest lithosphere (cratons; average dVs $\geq 4\%$); yellow? thinnest, warmest lithosphere (tectonically active or thinned; dVs $\leq -1\%$), and light blue?intermediate lithosphere (stable non-cratonic platforms or oceanic lithosphere; dVs 1-4%). Grey polygons represent plate boundaries. The location of the plume stem in the TZ (computed as average -1% dVs at 410-600 km depth) is shown as a dashed black contour, and is assumed to be stationary in the mantle. Dated extrusive igneous rocks[25] are shown as red circles. LIPs are shown as red polygons. Moving[71] and static hotspot tracks for Iceland are yellow and cyan diamonds and lines, respectively. Reconstructions are performed using rotations from[58].